Integrating thermodynamic and dynamic views on the control of the top-heaviness of convection in the Pacific ITCZ with weak temperature gradient simulations

Miguel Bernardez[1], **Larissa Back**[1]

[1]University of Wisconsin-Madison, Madison, Wisconsin

Key Points:

- Climatological bottom-heavy versus top-heavy vertical motion profiles in the boxes examined can be simulated from temperature profiles.
- These thermodynamic controls of vertical motion can be understood using a simple entraining plume model.
- The influence of SST gradients on vertical motion can be simulated via effects on the temperature profile.

Corresponding author: Miguel Bernardez, bernardez@wisc.edu

Abstract

Understanding what controls vertical motion profile shape is fundamental to understanding tropical precipitation patterns. Two controls have been previously studied: the thermodynamic profiles of the environment and the dynamics imposed by sea surface temperature (SST) patterns. To fit these two perspectives together, we focus on two regions with distinctly top and bottom-heavy vertical motion: The Western Pacific and the Central Eastern Pacific. These regions have roughly the same column-integrated water, precipitation, and column-integrated horizontal moisture advection, however the shape in the West is top heavy while the East is bottom heavy. The top-heaviness angle is introduced to describe this difference.

To study thermodynamic controls on vertical motion profile shape, we use weak temperature gradient (WTG) simulations. We are able to simulate the shape differences between our two regions from the thermodynamics. We then show that the dry static stability and the underlying SST are the most important for the vertical motion shape differences between our two regions.

We show that the qualitative shape differences can be explained using a simple entraining plume model. The entraining plume model accepts the temperature and moisture profiles as inputs and outputs the plume's buoyancy, which is directly related to the vertical motion profile shape. We find that increasing the dry static stability leads to bottom-heaviness. We hypothesize that the SST gradients lead to a cooler equilibrium lower tropospheric temperature compared with no gradient, and this leads to a more conducive thermodynamic environment to bottom-heaviness. Hence the dynamics control top-heaviness through influencing the thermodynamic profiles.

Plain Language Summary

In the tropics, the vertical velocity is related to the amount of rainfall in a region. There are large differences in the vertical velocity at different heights in different regions, which are important to the rainfall distribution. When upward vertical motion is faster lower in the atmosphere, the vertical motion is bottom-heavy. When it is faster higher in the atmosphere, the vertical motion is top-heavy. Some work indicates that these differences come from temperature profile differences and how adjacent regions change the moisture profile. Alternative work suggests that top-heaviness depends on the distribution of sea surface temperatures (SST). We use a model that predicts vertical motion to reconcile these two. We simulate top and bottom-heavy vertical motion profiles from just the differences in the thermodynamics of two regions. We then check what parts of the thermodynamics are most important to the vertical motion profile shape by changing one at a time and seeing how vertical motion changes. We find that temperature and SST are the most important factors, with bottom-heaviness being due to having a lower sea surface and a more stable temperature profile. We hypothesize that the SST distribution affects the temperature profile, which leads to more bottom-heaviness.

1 Introduction

Our understanding of the tropical rainfall distribution is limited because it entails interactions between many different systems across a multitude of scales, from cloud clusters (Yanai et al., 1973) to large-scale features like the Madden-Julian Oscillation (MJO) (Madden & Julian, 1971) to the slowly evolving climatological state (Riehl & Malkus, 1958). Vertical motion plays a central role in this problem and to the tropical rainfall distribution because it is directly tied to latent heating from rain through the dry static energy (DSE) budget(Yanai et al., 1973; Handlos & Back, 2014). The shape of the vertical motion profile in particular, is essential to how the tropical system behaves across

a range of timescales and waves (Schumacher et al., 2004; Back & Bretherton, 2006; Kang et al., 2009; Gjorgjievska & Raymond, 2014; Sherwood et al., 2014; Inoue & Back, 2015; Inoue et al., 2020).

Despite the importance of vertical motion profile shape to the tropical atmosphere, our understanding of the underlying processes that determine this shape is incomplete (Hagos et al., 2010; Back et al., 2017). In this work, we examine and integrate two mechanisms that have been proposed, in the literature, for how vertical motion is controlled. We do this in order to improve our ability to properly simulate the tropics. We look to create process oriented diagnostics (PODs) which can help us improve our diagnosis of vertical motion in models (Maloney et al., 2019). Our goal is to develop our understanding of the controls of vertical motion, which will then be used to create PODs and ultimately improve our models and our ability to forecast the tropics.

In this research, we focus on the causes of the difference between a region with climatological top-heavy vertical motion, where maximum vertical velocity is in the upper troposphere, versus a region with bottom-heavy vertical motion where the maximum vertical motion occurs in the lower troposphere. We use the regions found by Back and Bretherton (2006) to have consistently top-heavy or consistently bottom-heavy vertical motion: the Western and Central-Eastern Pacific boxes (shown in figures 1 and 3). These regions are chosen because reanalyses and AGCMs agree on whether they are top heavy or bottom heavy (see Back and Bretherton (2006)), while in many other regions and times throughout the tropics there is much less agreement between models and different observationally derived products. Figure (1a) shows the top and bottom-heavy vertical motion profiles, which are a result of the different conditions between the two regions. Both of our chosen regions have similar amounts of rainfall, column water vapor, and horizontal moisture transport and yet they achieve this energetically in different ways due to the different vertical motion shapes (Back & Bretherton, 2006). Throughout the rest of the paper we will refer to variables from the Central-Eastern Pacific box as bottom heavy and we will refer to the variables from the Western Pacific box as top heavy, so the top-heavy SST is the SST from Western Pacific box.

Figure (1 c) shows the climatological pattern of top-heaviness throughout the tropics using a new measure that we have created called the top-heaviness angle. This top-heaviness angle is an extension of the top-heaviness ratio created by Back et al. (2017), which utilizes the first two modes of a vertical decomposition of the vertical motion. The first two modes when the vertical motion is decomposed into a set of empirical orthogonal functions are responsible for greater than 85% of the vertical motion variability (Back & Bretherton, 2009b; Back et al., 2017). The ratio of the second to the first mode provides a compact representation of the top-heaviness which has been normalized by magnitude of vertical motion. The top-heaviness angle is found by taking the arctangent of this ratio, which gives an angle representation of the top-heaviness. The top-heaviness angle has the benefit of being well defined for all vertical motion, as opposed to being defined for either upward or downward vertical motion. The legend for the top-heaviness angle and the colormap that we use to visualize it are shown in figure (1b). Angles near zero represent strongly ascending regions, while angles near 180° represent descending regions. Positive angles near zero represent more top-heavy profiles and negative angles near zero represent more bottom-heavy profiles.

Previous research has identified two mechanisms that control the climatological distribution of top-heaviness shown in figure 1. The first mechanism depends partially on surface convergence caused by the distribution of SSTs, which we call the dynamic mechanism (Lindzen & Nigam, 1987; Back & Bretherton, 2009a, 2009b; Duffy et al., 2020). The second mechanism, which we call the stability mechanism, focuses on the role of the large-scale thermodynamics (Raymond & Sessions, 2007; Raymond et al., 2015; Sessions et al., 2019).

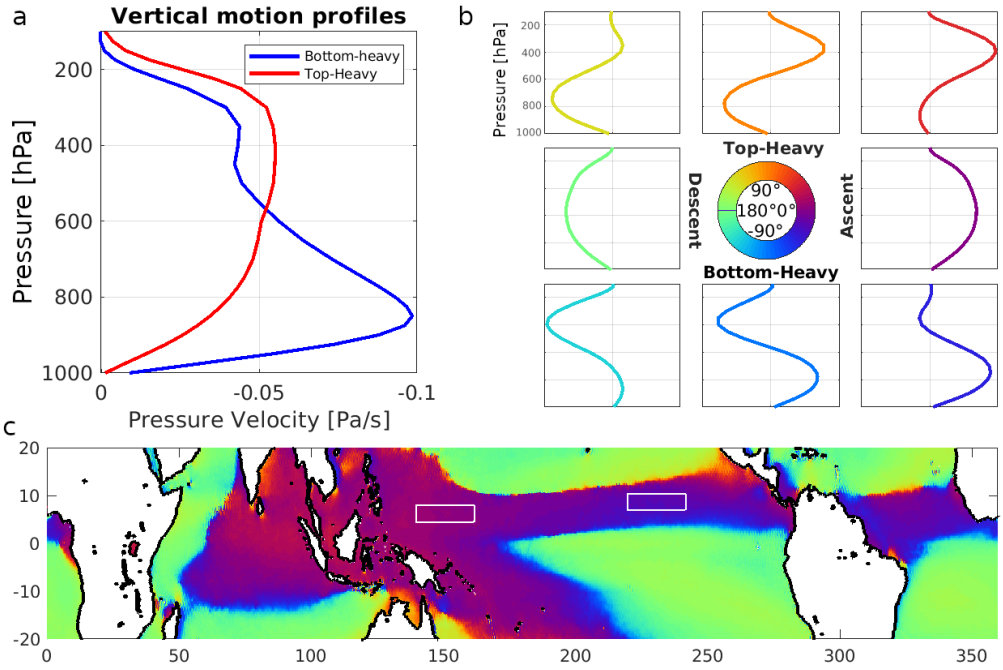

Figure 1. Geographic variability of vertical motion in the tropics is shown with the top-heaviness angle, along with the vertical motion from the top and bottom-heavy boxes that we are studying and a legend to understand the top-heaviness angle. (a.) Top and bottom-heavy vertical motion profiles from the two indicated boxes, which serve as the regions of interest for this study. (b.) Color legend showing variability of vertical motion shape according to top-heaviness angle. (c.) Map of the variability of vertical motion shape shown using the top-heaviness angle over the tropics for the ERA5 climatology between 2007-2017.

The dynamic mechanism describes the top-heaviness using the surface conditions, specifically the distribution of SSTs and the laplacian of SST which indicates where the gradients of SST drive the greatest boundary layer convergence (shown in figure 3). The SSTs in the top-heavy box are around 2K higher and the laplacian of SST in the bottom-heavy box indicates greater convergence.

The dynamic mechanism begins with a surface convergence that is caused by SST gradients, diagrammed in figure (2)(Lindzen & Nigam, 1987). SST gradients lead to boundary layer temperature gradients which lead to bent isobars in the boundary layer. In association with friction, these bent isobars lead to a convergent flow and vertical motion near the surface. Back and Bretherton (2009b) found that in the bottom-heavy box, the monthly and longer time-averaged surface convergence, and thus lower tropospheric vertical motion, is primarily due to the SST gradients on these timescales. Their companion paper Back and Bretherton (2009b) argued that the greater top-heaviness of vertical motion in the top-heavy box, compared to the bottom-heavy box, is attributable to the difference in relative SST in the two regions (Back & Bretherton, 2009a). A higher SST is correlated with a greater atmospheric potential energy, which is associated with deeper and thus more top-heavy vertical motion. The magnitude of the SST and its gradients can be used to create a simple model that predicts the distribution of vertical motion shape and precipitation in reanalysis and GCMs (Back & Bretherton, 2009a, 2009b; Duffy et al., 2020). The Back and Bretherton (2009b) model clearly has strong explanatory power, but the precise way that the SST and its gradients exert control over the top-

heaviness, from the perspective of the thermodynamics, has not been determined and a goal of this research is to elucidate the subject.

The stability mechanism describes how vertical motion is controlled by the large-scale thermodynamic environment and predicts bottom-heaviness as a consequence of having a more stable temperature profile. The reason for this is an implicit relationship to plume buoyancy, but the details of this have not been studied in depth. We investigate this further in section 4. The stability mechanism was first uncovered and explained using a simplified model of large-scale vertical motion where stabilizing the large-scale environmental temperature led to the vertical motion becoming more bottom-heavy (Raymond & Sessions, 2007; Sessions et al., 2015). In contrast, when the large-scale temperature is destabilized, the vertical motion becomes more top heavy. These simulations indicated the existence of the stability mechanism, which was then supported by observations from several field campaigns (Gjorgjievska & Raymond, 2014; Raymond et al., 2014; Sessions et al., 2019).

Both of these mechanisms offer an explanation for bottom-heavy vertical motion, and both mechanisms have unanswered questions that leave holes in our understanding. Whether the dynamic mechanism acts through influencing thermodynamic profiles is still unknown. The stability mechanism's role in the climatological top-heaviness has not been previously demonstrated and additionally, it does not provide an answer to why the top and bottom-heavy boxes have similar amounts of rainfall and column moisture while having different vertical motion profiles.

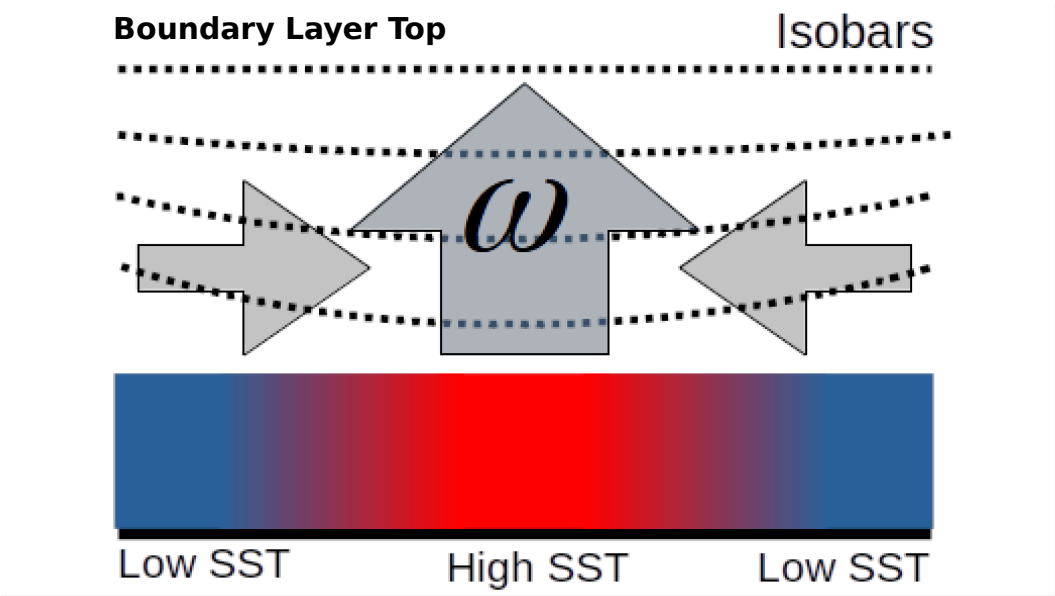

Figure 2. Schematic of the SST gradient driven surface convergence and how it generates vertical motion. Horizontal SST gradients imprint on the boundary layer. In association with friction, these pressure gradients generate convergent winds. These convergent winds are associated with upward vertical motion in order to satisfy mass continuity. This process is important to regions with bottom-heavy vertical motion according to the dynamic mechanism.

We use simulations from a model that parameterizes vertical motion using the weak temperature gradient (WTG) approximation, which is the same parameterization which helped uncover the stability mechanism (Raymond & Sessions, 2007; Sessions et al., 2015; Raymond & Flores, 2016; Sentić et al., 2015). We use a particular implementation of the

WTG approximation called the spectral WTG (SWTG) parameterization that has been shown to reproduce vertical motion from observations as well as the stability mechanism (Herman & Raymond, 2014; Wang et al., 2016). We are using reanalysis data instead of observations to simulate climatological vertical motion profiles, because they are the most continuous and accurate data available on climatological timescales. We wish to understand the mean behavior, so we use time-independent boundary conditions from the climatology values. We simulate the environments and resulting vertical motion from our top and bottom-heavy boxes in order to answer the following questions:

- Can the top-heaviness differences between our two regions be simulated from the SST, temperature profile, and horizontal moisture advection profile or do we need to additionally impose the dynamic mechanism?
- If so, what are the most important thermodynamic factors in determining vertical motion shape and its geographic variability?
- Can we connect the vertical motion shape to the environment using a simple entraining plume model?
- How can we reconcile the dynamic and stability mechanisms in light of the results we obtain?

The paper is laid out as follows: In the next section we will discuss the details of the WTG model that we use and the initial simulations of the two regions. Following that we will explore the sensitivity of the top-heaviness to different aspects of the thermodynamics in order to uncover the most important aspects. After this we will use a simple model of an entraining plume in order to explain the thermodynamic controls of vertical motion. Finally we will discuss how the two mechanisms are linked together and propose a unified mechanism for the control of top-heaviness.

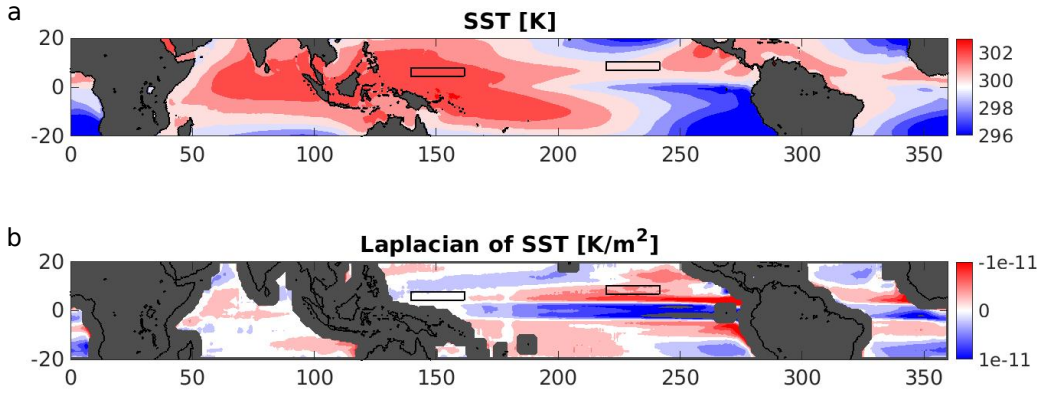

Figure 3. Map of the surface characteristic variability important to setting the vertical motion profile shape according to the dynamic and stability mechanism. (a.) map of the SST [K] for the 10 year ERA5 climatology. (b.) The laplacian of SST of the above plot, areas with negative values, colored here in red, are areas where the SST pattern will drive convergence $[K/m^2]$.

2 Weak Temperature Gradient Simulations

2.1 WTG parameterization

The WTG approximation, at its most basic, is that horizontal temperature gradients, and thus horizontal temperature advection, can be ignored because they are much

smaller than the other important factors (Sobel et al., 2001). The small Coriolis force in the tropics means temperature anomalies are quickly redistributed by gravity waves which leaves horizontally homogeneous temperatures. When there is no horizontal advection of temperature, vertical advection becomes the primary balance for diabatic heating which makes the WTG approximation incredibly useful as a simplifying assumption to the virtual potential temperature budget equation:

$$\frac{\partial \theta_v}{\partial t} + \vec{v} \cdot \nabla \theta_v = Q. \tag{1}$$

In this equation, θ_v is the virtual potential temperature, $\vec{v}$ is the 3D wind velocity vector, and Q is the diabatic heating. We simplify by first neglecting the horizontal advection term using the WTG approximation. We also assume the time tendency is zero because we are considering the mean behavior. This makes the new virtual potential temperature equation:

$$W \frac{\partial \theta_v}{\partial z} = Q. \tag{2}$$

The vertical motion is an important aspect of the diabatic heating, which makes forecasting in the tropics a tricky affair without something like our small domain cloud resolving model (CRM) which simulates the diabatic heating. We use the virtual potential temperature change that results from this heating to calculate the WTG vertical motion. Specifically, we replace the diabatic heating in the above equation with the difference in virtual potential temperature between the model domain mean, $\overline{\theta_v}$, and the prescribed profile, θ_v^b, divided by a characteristic relaxation time scale τ. The prescribed virtual potential temperature profile is taken from a special simulation which is discussed in more detail in the next section. We then solve for the vertical motion, giving us our WTG velocity equation:

$$W_{WTG} = \frac{\overline{\theta_v} - \theta_v^b}{\tau(\partial \theta_v / \partial z)}. \tag{3}$$

The model advects virtual potential temperature and moisture vertically according to this WTG vertical velocity, driving the model evolution towards equilibrium.

We use a particular implementation of the WTG parameterization, called spectral WTG (SWTG), that decomposes the vertical motion into a series of vertical modes and their amplitudes. Each of these modes individually redistribute anomalies at a characteristic time-scale determined by the mode. The virtual potential temperature anomaly that each mode relaxes to is found by projecting the total virtual potential temperature anomaly onto the mode. Putting this together, the SWTG velocity is found using:

$$W_{SWTG} = \sum_j \langle \frac{\overline{\theta_v} - \theta_v^b}{\tau_j(\partial \theta_v / \partial z)}, \Omega_j \rangle \frac{\Omega_j}{\langle \Omega_j, \Omega_j \rangle}. \tag{4}$$

Where τ_j is the mode specific relaxation time, Ω_j are the vertical modes, and $\langle\rangle$ indicates a mass-weighted column integral. This method of parameterizing the vertical velocity is more realistic and provides better results with fewer assumptions than earlier implementations (Herman & Raymond, 2014). The mode specific relaxation time-scale is found using the following equation:

$$\tau_j = \tau_1 (c_n / c_1)^{-1}. \tag{5}$$

In this equation, c_n is the wave speed of the specific mode, c_1 is the wave speed of the first mode, and τ_1 is the relaxation time-scale of the first mode, which is set as a parameter of the model.

2.2 Horizontal Moisture Advection

We still have to consider the horizontal transport of moisture in and out of the domain, even though the horizontal advection of temperature is negligible. There are four methods of moisture transport that have been used in previous WTG simulations: moisture relaxation (Sobel et al., 2007), lateral moisture entrainment (Raymond & Zeng, 2005), moisture ventilation (Raymond & Fuchs-Stone, 2021) and imposed moisture advection (Sobel & Bretherton, 2000; Wang et al., 2016). The first three of these methods represent aspects of horizontal moisture transport that are locally forced. However, a considerable amount of horizontal moisture transport can be driven by non-local processes which are outside of the scope of our model (see Appendix A of Wang et al. (2016)).

Because of the potential for one of the other parameterizations to miss important non-local variability, we choose to use the fourth method and impose the profile of horizontal advection from the reanalysis. The horizontal moisture advection is calculated using

$$Q_{qhadv} = -\vec{v_h} \cdot \nabla q_v, \tag{6}$$

where q_v is the specific humidity, v_h are the horizontal winds, and Q_{qhadv} is the horizontal moisture advection.

The horizontal moisture advection can influence the vertical motion profile and the balance between moisture and vertical motion (Sessions et al., 2016; Wang & Sobel, 2012). The methods other than imposing the observed horizontal moisture advection are attempts to parameterize important aspects, and ultimately capture, the horizontal moisture advection. Imposing the horizontal moisture advection that existed in balance with the vertical motion is the simplest way to achieve our goal of recreating the environment in order to simulate the vertical motion profile. We also do not have to worry about imposing a large-scale moisture profile that corresponds to what is occurring in adjacent columns to the area of interest.

2.3 Model setup

We generate our simulations in essentially the same way as Wang et al. (2016) with the modification that our boundary conditions are time-invariant and we run to a steady state, instead of simulating a discrete time-series. The WRF model (version 3.5.1) (Skamarock et al., 2008) is used as the basis for our WTG model. The model has a lower bound of the mean SST, doubly periodic lateral boundary conditions, and an implicit damping scheme is used as the upper boundary condition (Klemp et al., 2008). We use a domain size of 64km×64km×23km with a grid size of 1 km. We use 60 stretched vertical levels with 10 levels in the first kilometer. The WTG relaxation time scale that we use for the first mode is 1 hour.

In addition to the large-scale temperature, which is integral to the WTG parameterization, we also impose the large-scale profile of horizontal winds and relax the domain average wind profiles towards the large-scale winds, with a relaxation time of 1 h. The parameterization of the microphysics is done using the Morrison two-moment scheme (Morrison et al., 2009). The parameterization of the interactive radiation using the RRTMG long-wave scheme and the Goddard shortwave scheme (Iacono et al., 2008) with a constant solar insolation of 370w/m^2 (Chou & Suarez, 1999; Matsui et al., 2007; Shi et al., 2010). We parameterize subgrid scale eddies using the three-dimensional Smagorinsky first-order closure scheme and an implicit vertical diffusion scheme is used to ensure numerical conservation of moisture. Everything else that we have not mentioned is kept the same as Wang et al. (2016).

The SWTG parameterization calculates the vertical velocity profiles as a function of the large-scale temperature profile. Due to the mismatch between real-world physics and the model physics, we cannot compare the profiles of temperature directly to each

other. We solve this issue by using a model analogue for the large-scale temperature instead of using the reanalysis temperature profile. Many previous WTG simulations, especially simulations of steady states, have used radiative convective equilibrium (RCE) states as the primary source of the environmental temperature profiles (Raymond & Sessions, 2007; Wang et al., 2013; Daleu et al., 2015; Anber et al., 2015). However, the presence of large-scale vertical motion alters that temperature profile relative to RCE (Singh et al., 2019a). To fix this problem, instead of running the model under RCE conditions, we run the model with the vertical motion from reanalysis in place of the WTG parameterization and recover the large-scale temperature profile that is in balance with this vertical motion profile. This is similar to the methods used by Edman and Romps (2015) and Wang et al. (2016).

We call these simulations the driven equilibrium (DE) simulations, because we allow the observed advection to drive our model to an equilibrium that is equivalent to the reanalysis climatology. There is a discrepancy between the DE temperature profile and the profile that we want to use caused by the presence of the large-scale vertical motion. This can be seen if we rewrite the WTG velocity equation as

$$\theta_v^b = \overline{\theta_v} - \tau W \frac{\partial \theta_v}{\partial z} \tag{7}$$

The DE simulation outputs $\overline{\theta_v}$ and we wish to use θ_v^b in our simulations. We solve for θ_v^b using the above equation and use it in the SWTG simulations as the large-scale temperature profile. The temperature correction that we add is small and dependent upon the timescale that is used.

In addition to the temperature profile, we also take the moisture and radiative heating profile from the DE simulations. We use the moisture profile to initialize the model and we use the radiative heating profile instead of interactively simulating it, which helps to avoid dry equilibrium cases (Sessions et al., 2016).

2.4 Model Validation

We first validate that our configuration of the model is able to simulate mean vertical motion profiles. We recreate the original DYNAMO simulations from Wang et al. (2016), which are shown in figure (8), with the version (1) data from the northern sounding array (Johnson & Ciesielski, 2013; Ciesielski et al., 2014). To validate that our model setup performs similarly, we also run simulations where we remove the time-dependence from the model input and replace it with its average. Some details and results of the DYNAMO validation simulation along with the later simulations are found in tables 1 and 2. The first table shows the base simulation along with the source of the SST, radiative heating profile, temperature profile, and moisture advection profile. The first three simulations in the list are the DYNAMO validation simulations and the other two groups of simulations are of the top and bottom-heavy boxes and will be discussed later. The second table shows the precipitation, top-heaviness angle, surface latent heat flux, column integrated radiative heating, and SF. We found that the time-independent boundary conditions are able to generate vertical motion profiles that are similar to the time-dependent simulations and to the observations. This gives us confidence that the model is able to produce the long-term mean vertical motion from a mean thermodynamic environment.

We next test that our model produces the vertical motion shape response to the large-scale temperature anomalies that is the basis for the stability mechanism (Raymond & Sessions, 2007; Sessions et al., 2015). We test this by adding two temperature perturbations, which we have taken from the previous research, to the large-scale temperature profile and simulating vertical motion profile response. The results, which can be seen in figure (7) and will be discussed later, show that when we apply a stabilizing temperature anomaly, the vertical motion transitions from top heavy/neutral to bottom heavy.

The reverse occurs when we apply a destabilizing temperature anomaly; this leads to a stratiform vertical motion profile that is extremely top heavy. We used an interactive radiation scheme in these simulations and an imposed radiative heating profile for the rest of the simulations in this paper, however this choice should not be impactful because the choice has been shown to be unimportant to the stability mechanism (Sessions et al., 2016).

The model displays the correct vertical motion response to the temperature anomaly, but the response of the moisture profile is not consistent with what has previously been seen in Raymond and Sessions (2007), Sessions et al. (2015), and Sentić et al. (2015). In their work, they saw a correlation between the stability and column moisture, with greater stability leading to greater column moisture. While we do see a moisture profile response for all three profiles (figure 7c), they have nearly identical column moisture. We discuss the reasons for this further in section (7).

Base SWTG Simulation	Radiation source	SST source	Stability source	Moisture Advection source
1. DYNAMO	interactive	average	time-independent	time-independent
2. DYNAMO	interactive	average	stable	time-independent
3. DYNAMO	interactive	average	unstable	time-independent
4. Top-Heavy	top-heavy	top-heavy	top-heavy	top-heavy
5. Top-Heavy	top-heavy	bottom-heavy	top-heavy	top-heavy
6. Top-Heavy	top-heavy	top-heavy	bottom-heavy	top-heavy
7. Top-Heavy	top-heavy	top-heavy	top-heavy	bottom-heavy
8. Top-Heavy	bottom-heavy	top-heavy	top-heavy	top-heavy
9. Bottom-Heavy	bottom-heavy	bottom-heavy	bottom-heavy	bottom-heavy
10. Bottom-Heavy	bottom-heavy	top-heavy	bottom-heavy	bottom-heavy
11. Bottom-Heavy	bottom-heavy	bottom-heavy	top-heavy	bottom-heavy
12. Bottom-Heavy	bottom-heavy	bottom-heavy	bottom-heavy	top-heavy
13. Bottom-Heavy	top-heavy	bottom-heavy	bottom-heavy	bottom-heavy

Table 1. The list of SWTG simulations that were run along with where the data came from and how it differs between runs. The base simulation is the starting simulation to which changes are applied. The base simulations include the DYNAMO simulation for the validation tests and the basic top and bottom-heavy SWTG simulations. The variables that we change are the radiation, SST, dry static stability, and horizontal moisture advection profile.

3 Top/Bottom-heavy simulations

3.1 Reanalysis

We start with a test to see how well we can simulate the vertical motion from the thermodynamic differences between our two regions. We use the ERA-5 reanalysis as the source of our climatology data. We utilize data on both pressure levels and single levels (Hersbach et al., 2019a, 2019b) over the time span of 2007-2017. The top and bottom-heavy boxes that we are studying from Back and Bretherton (2006) have bounds of 5-7.5 °N 140-160°W for the top-heavy region and 7.5-10°N 120-140°E for the bottom-heavy region. We construct our long term mean by averaging daily data. The thermodynamic profiles that we use to run the model are temperature, water vapor mixing ratio, horizontal winds, profiles of vertical velocity and horizontal moisture advection. The wa-

Simulation	Rain (mm/day)	ϕ_{TH} (°)	SLH (w/m^2)	$\langle Q_R \rangle$ (w/m^2)	SF
1.	8.4	6.1	120.3	-69.2	0.84
2.	14.0	-43.0	150.2	-144.6	0.84
3.	9.3	62.9	99.6	-36.0	0.84
4.	7.8	0.2	143.4	-61.9	0.81
5.	0	153.4	188.8	-64.4	0
6.	29.8	23.4	183.0	-61.6	0.88
7.	5.9	-2.2	151.4	-61.9	0.81
8.	8.9	-6.5	140.7	-80.8	.81
9.	6.1	-46.3	104.9	-80.7	0.83
10.	27.8	24.7	192.0	-80.2	0.89
11.	0	167.4	165.9	-81.2	.04
12.	11.3	-13.4	91.7	-80.6	.86
13.	5.04	-44.9	110.9	-62.14	.813

Table 2. The rain, top-heaviness, surface heat fluxes and radiation for the previously listed SWTG simulations.

ter vapor mixing ratio profiles are only used to generate the horizontal moisture advection profiles and to initiate the DE simulations.

The horizontal moisture advection that we impose in our simulations is calculated using a center difference method on pressure levels from daily data, which is then averaged to the 11 year climatology. Both profiles act as drying terms in the moisture budget. However, they have distinct vertical profiles (see figure (4 d). The bottom-heavy box has almost all of its advection concentrated near the surface. The top-heavy box, meanwhile, has a profile of moisture advection that is fairly consistent through a deeper layer of the troposphere.

The difference in temperature profiles between the two boxes is shown in figure (4a). The bottom-heavy box is 2K cooler than the top-heavy box at both the surface and near the tropopause. The SST in the bottom-heavy box is also around 2K cooler than the top-heavy box, which is the likely reason for much of the difference in temperature profiles. The bottom-heavy box has a slightly higher relative humidity in the lower troposphere where there is more vertical motion. Meanwhile, the top-heavy box has greater relative humidity in the upper troposphere where it begins to have greater vertical motion. Also shown in figure (4) are the equivalent temperature and moisture differences that our model produces, which are discussed in the following section.

3.2 Driven Equilibrium simulations

The driven equilibrium (DE) simulations are our model's analogue to climatology. The DE has alternatively been called radiative convective dynamic equilibrium (RCDE) by Singh et al. (2019a) and radiative convective advective equilibrium (RCAE) by Romps (2021). Table 3 shows the DE results along with the observation and reanalysis that the model is trying to replicate. The table shows measures which are important to the energy budget including the rain rate, the column radiative heating, the surface latent heat flux, and our newly introduced top-heaviness angle to measure the vertical motion profile shape.

We produce our own estimates of precipitation consistent with the vertical advection that we are interested in, which allows us to compare the precipitation between different sources and to combat potential biases in the estimates. Taking the column in-

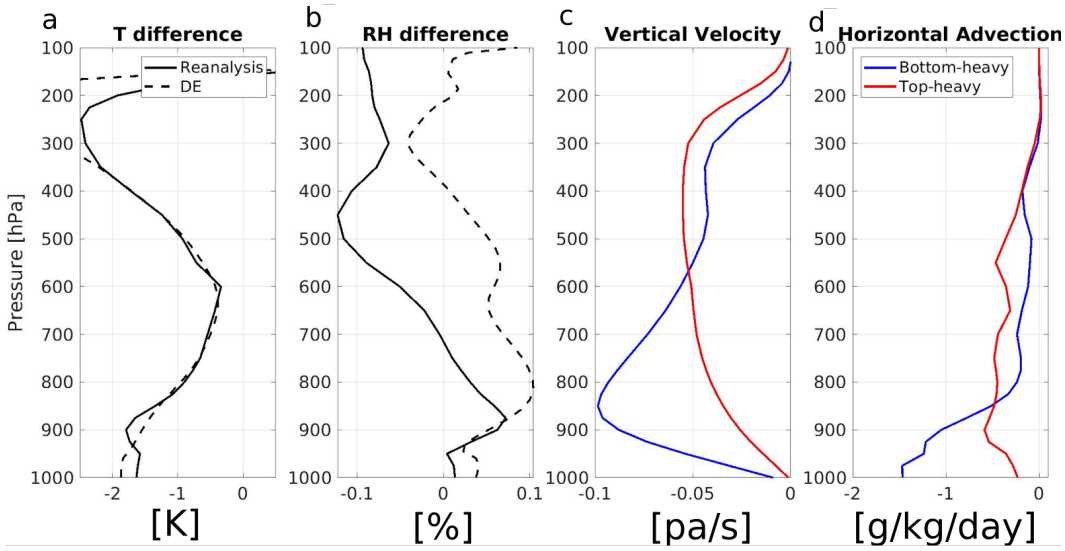

Figure 4. The large-scale thermodynamic environment used to simulate the vertical motion shape from reanalysis and DE simulations. (a.) Temperature difference between the bottom-heavy box and top-heavy box for both reanalysis and the DE simulations. The negative values show that the top-heavy box is warmer throughout the column. (b.) This shows the RH differences between the bottom and top-heavy boxes from both reanalysis and the DE simulations. (c.) Vertical motion profiles, in units of $[Pa/s]$, for our two regions. (d.) Horizontal moisture advection calculated using daily data for each day in the time span then averaged.

tegrated DSE budget equation along with the WTG assumptions, no storage or horizontal advection of DSE, and assuming that surface sensible heat fluxes are negligible, DSE storage or horizontal advection allows us solve for precipitation:

$$P = \langle \omega \frac{\partial s}{\partial p} \rangle - \langle Q_R \rangle \tag{8}$$

Here P is the precipitation, s is the DSE, and $\langle Q_R \rangle$ is the column integrated radiative heating. These precipitation estimates are a useful metric for comparing how close the models are to each other and to the real world. If a model is accurately representing physics the estimate of precipitation should match with the observed precipitation. The precipitation values that we calculate for each of the data sets and the DE simulations can be found in table (3).

Figure (4a and b) also shows the differences in temperature and moisture between the top and bottom-heavy boxes for the DE simulations, along with the reanalysis profiles. The DE simulation is able to capture the lower tropospheric temperature differences well between the two regions. The upper troposphere shows disagreement between the DE temperature profile and reanalysis, which is most likely caused by the model's artificial lid. Overall there is a close match between the temperature profile differences in reanalysis and our DE simulations.

The moisture differences are much more significant, showing a bottom-heavy box that is relatively too moist compared to the top-heavy box throughout the column. The bottom-heavy box has a greater relative humidity than the top-heavy box throughout a much more significant portion of the atmosphere. This is reflected in the precipitation rates differences, which can be seen in table (3). The bottom-heavy DE simulation has

	Rain (mm/day)	top-heaviness $\phi_{TH}(^\circ)$	surface latent heat flux SLH (W/m^2)	column radiative heating $\langle Q_r \rangle (W/m^2)$
DYNAMO (observation)	8.89	9.42	103.0	not available
DE simulation	9.73	N/A	110.7	-68.8
Top-heavy (Reanalysis)	9.63	1.55	131.2	-75.7
DE simulation	8.6	N/A	145.0	-63.0
Bottom-heavy (Reanalysis)	8.29	-24.5	126.5	-89.1
DE simulation	10.6	N/A	110.7	-78.7

Table 3. Data from observation and reanalysis alongside the data from the DE simulations. Shown are the rain in mm/day, the top-heaviness angle, the surface latent heat flux and column radiative heating.

greater rain than the top-heavy DE simulation, which is the reverse of what we see in reanalysis.

We also show variables relating to column energy, surface latent heat flux and radiation, in table (3). The DE simulations capture the relative differences in radiative heating between the two regions well, with both columns producing less radiative cooling than reanalysis. The surface latent heat flux differences between the top and bottom-heavy domain are also similar to reanalysis but the differences are much larger. This surface heat flux difference explains around half of the column MSE difference implied from the different rain rates.

The DE simulations match the reanalysis closely enough that our model provides useful results and we move on to addressing our primary research questions. The importance of the minor differences between the DE simulation and the reanalysis are beyond the scope of the current research. Our next step is to simulate the vertical motion profiles to see if the WTG parameterization captures the vertical motion differences.

3.3 SWTG top/bottom-heavy simulations

The simulated vertical velocity profiles from the top and bottom-heavy simulations, presented in figure (5), show that the climatological vertical motion profile shapes, and importantly, bottom-heavy vertical motion, can be simulated using the thermodynamic profiles as boundary conditions. Table (1) shows all of the simulations and their parameters. The first group are the validation simulations that we ran while the next two groups of simulations are of the top and bottom-heavy boxes. The first simulation in each of the top and bottom-heavy lists is the basic simulation, while the next four are the sensitivity simulations that will be discussed later. Table (2) shows the same model output variables as table (3) with the addition of the saturation fraction (SF), which is the ratio of the column integrated moisture to the column integrated saturation moisture, which is also known as the column relative humidity (Bretherton et al., 2004). The simulation of the bottom-heavy box, simulation 9, produced vertical motion with a top-heaviness angle of -46°, see table (2). The simulation of the top-heavy box, simulation 4, has a vertical motion profile similar to the reanalysis profile, although not as top heavy, with an angle of 0° compared to 15° in reanalysis (See table 3 for reanalysis data).

The precipitation rates that the SWTG simulations produce are lower than both the reanalysis and DE rain rates (table 3). Both simulations have similar deviations from the reanalysis rain rate which come primarily from differences in the vertical motion profile shape. In the bottom-heavy simulations, the difference between the reanalysis sur-

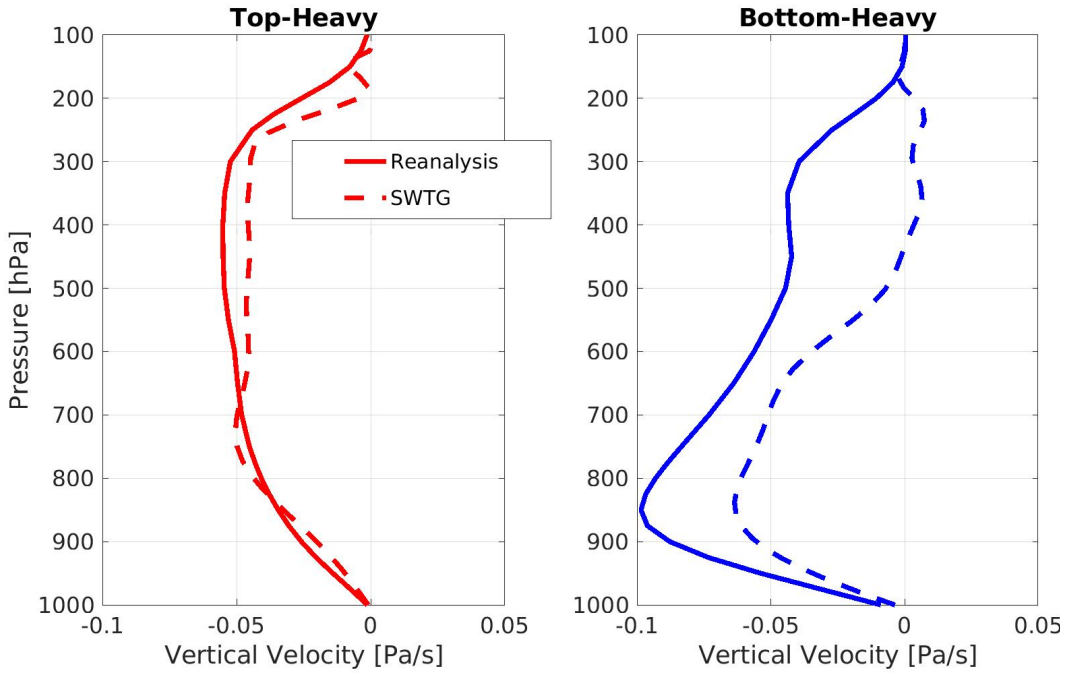

Figure 5. Vertical motion profiles simulated in top and bottom-heavy domains show that the thermodynamic environment alone can determine top-heaviness qualitatively correctly in simulations. The solid lines are the climatology profiles from ERA5 reanalysis. The dashed lines are the cases with imposed radiation, where we use the profile of radiative heating from the DE simulations.

face heat flux and the SWTG surface heat flux explains approximately 1/4 of the precipitation deviation. We also find the negative correlation between top-heaviness and column moisture that has been previously used as evidence of the stability mechanism; the top-heavy box has a lower SF than the bottom-heavy box. Despite this, we do not see the correlation between the precipitation and top-heaviness which was also used to evidence the stability mechanism (Raymond & Sessions, 2007; Sessions et al., 2015; Raymond et al., 2015; Sentić et al., 2015). We explain the reason for this difference further in section (7).

The ability of the model to simulate both bottom and top-heavy vertical motion demonstrates that the vertical motion shape is primarily controlled by large-scale thermodynamics. This compels us to ask what parts of the thermodynamic environment are most responsible for the vertical motion shape.

4 Thermodynamic sensitivity tests

We next run sensitivity tests, simulations 5-9 and 10-13, in order to determine which aspects of the thermodynamics are the most important to vertical motion profile shape. In each sensitivity simulation, we start with the initial and boundary conditions for either the basic top or bottom-heavy simulation domain and switch one of the following parameters: the large-scale temperature profile from the DE simulation, the moisture advection profile, the underlying SST, or profiles of radiative heating. This is shown in table 1 which shows the base SWTG simulation that is modified along with which modification is made to generate the sensitivity simulation. We then take an average of the vertical motion from each simulation that has a parameter in common, which gives us

four profiles of vertical motion from each. We then subtract the profiles from the two boxes in order to get the effective change caused by the difference between the boxes.

The effect on the vertical motion profile from the differences are shown in figure (6 A). We pick a parameter and average all of the vertical motion profiles from the simulations with that parameter and then subtract the top and bottom-heavy profiles. For example, the temperature sensitivity is found by averaging the simulations with the stability source labeled top-heavy (simulations 4,5,7,8,11), averaging those labeled bottom-heavy (simulations 5,9,10,12,13), and finally subtracting them. For the stability sensitivity, we switch the sign of the resulting vertical motion profile so that it represents a change from the top-heavy box to the bottom-heavy box, so that the sensitivity profiles represent an increase in stability.

When a simulation enters the dry equilibrium, rather than use the dry equilibrium vertical motion output in calculations of mean profiles, we use a vertical velocity that we calculate assuming it balances the radiative cooling. The dry equilibrium becomes unrealistically dry and the resulting vertical motion may also become non-physical. We calculate the velocity from the DE simulation temperature by dividing the radiative heating profile by the DSE stratification at each level.

The four parameters equate to eight additional test sensitivity simulations whose result can be seen in tables (1 and 2) as simulations 5-8 for the top-heavy cases and 10-13 for the bottom-heavy ones. There were two cases that entered into the dry equilibrium: simulation 10 which is the bottom-heavy box with the top-heavy temperature profile and simulation 5 the top-heavy box with the bottom-heavy SST. Both cases that went to the dry equilibrium had the lower, bottom-heavy SST and the more unstable, top-heavy temperature profile. We do not use the vertical motion profiles from these simulations, since they are non-physical, and instead use the vertical motion profile that is in balance with the radiative heating profile.

The two largest vertical motion profile changes came from the SST and the stability difference between our two regions, simulations 6 and 9 respectively. The vertical motion response from increasing the SST has very little change in vertical motion lower in the atmosphere and a large increase above the freezing level in the upper troposphere. The stability on the other hand, increases the vertical motion everywhere it is cooler, both the upper and lower troposphere. The moisture advection resembles the stability response with an increase in both the upper and lower troposphere. However the effect is much smaller than both of the others.

The results show that the radiative heating differences act as a feedback mechanism for vertical motion and convection and not as a primary forcing. The sensitivity of the vertical motion shape to the profiles of radiation is significantly smaller than either the stability or SST sensitivity effects. There is a small increase in the amount of vertical motion in the lower troposphere and decrease in the upper troposphere. This means the profile of radiative heating is contributing very slightly to the top-heaviness differences between the two boxes. The difference in radiative heating between the two simulated profiles is $10w/m^2$ on average, which is one third the difference in the surface latent heat fluxes. The vertical velocity that would balance the radiative heating differences is an order of magnitude smaller than the radiation sensitivity vertical velocity that is shown in figure (6) so this is not playing a significant role.

The difference due to horizontal moisture advection is also much smaller than the differences due to the SST and temperature profile. The horizontal advection from the top-heavy box induces greater vertical motion but does not affect the vertical motion profile shape much. This can partially be attributed to the differences in the vertical distribution of the moisture transport, because mid-level moistening is more effective than low level moistening in invigorating convection (Wang & Sobel, 2012). Another poten-

tial explanation for the lack of effect is that the column averaged horizontal advection of moisture is not significantly different between the two imposed profiles. If we were to choose two boxes with significantly different amounts of horizontal moisture advection, we might see a larger effect. The distinction between how the vertical motion profile shape and amplitude are altered by differences in both the vertical structure and the amplitude of horizontal moisture advection should be addressed by future research.

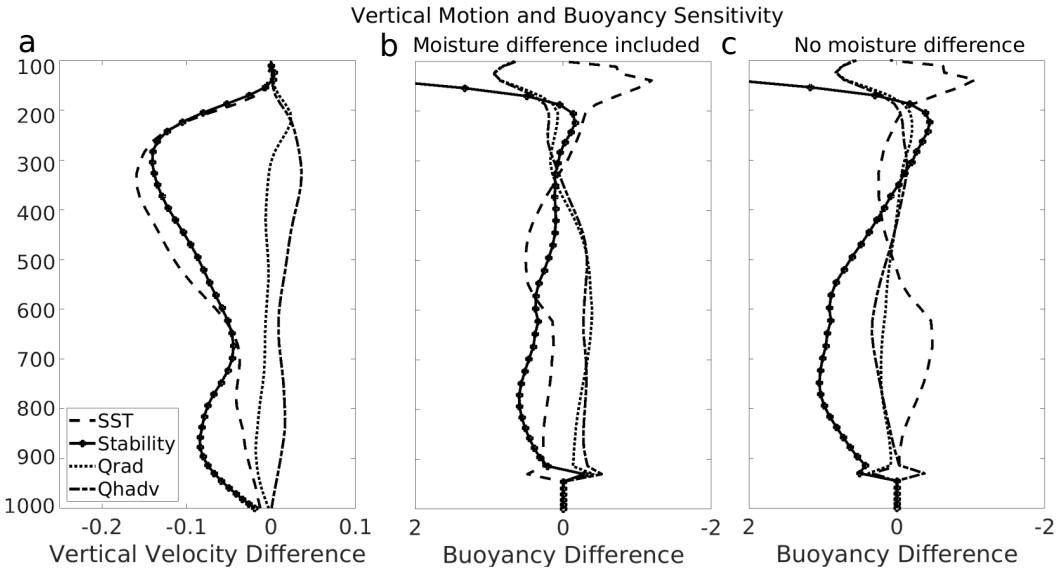

Figure 6. The average vertical motion shape (panel a) and plume buoyancy response (panels b and c) to thermodynamic variable differences between the top and bottom-heavy simulations. The vertical motion and plume buoyancy changes are most sensitive to SST and temperature profile variations and less sensitive to radiation and horizontal moisture advection. The sign of the stability change profiles have been reversed, which means it represents a change from the top-heavy to the bottom-heavy variable in question. The other three profiles, SST, radiation, and lateral moisture advection, represent a change from bottom heavy to top heavy. (b.) The plume buoyancy sensitivity with the RH differences between the two domains included. (c.) The plume buoyancy differences calculated using the mean RH profile so that the differences are due only to temperature differences.

We deduce that the bottom-heavy vertical motion in the Central Eastern Pacific, from the perspective of the thermodynamics, is due primarily to a combination of higher stability and lower SST, while the top-heavy vertical motion in the Western Pacific is due to a combination of high SSTs and low stability. The sensitivity tests with both high stability and warm SST became extremely top heavy with vigorous convection. This is consistent with the dynamic mechanism, which predicts that high SST will lead to top-heavy vertical motion profiles. The fact that the more stable simulations have higher humidity and rainfall is also consistent with the stability mechanism. However, the stability mechanism predicts bottom-heavy vertical motion in this case, which is not what we see in the simulations. Additionally, the dynamic mechanism says that the surface convergence due to SST gradients is essential but it is not explicitly present in our model, although it may be affecting the temperature profile we input as discussed in section 6.

5 An Entraining Plume Perspective

To understand how the control of SST and the temperature profile on vertical motion top-heaviness works, we turn to an entraining plume model. These models have a rich and storied history in tropical meteorology, and recently have been used to understand column-integrated water-vapor precipitation relationships (Singh & O'Gorman, 2013; Adames et al., 2021; Ahmed & Neelin, 2018; Abbott & Cronin, 2021; Singh et al., 2019a; Singh & Neogi, 2022), as well as the basis for one of the first convective parameterizations (Arakawa & Schubert, 1974). However, they have never been applied to the shape of the vertical motion profile. Hence this is a novel endeavor in which we believe that even qualitative relationships are a step forward from the existing knowledge-base. Our goal in this work is to understand why, from the perspective of a rising parcels buoyancy, more stable temperature profiles lead to more bottom-heavy vertical motion profiles. In the following section we will discuss our plume model and what it tells us about the thermodynamic controls of top-heaviness. Then, we turn to how we can reconcile the stability mechanism and dynamic mechanism.

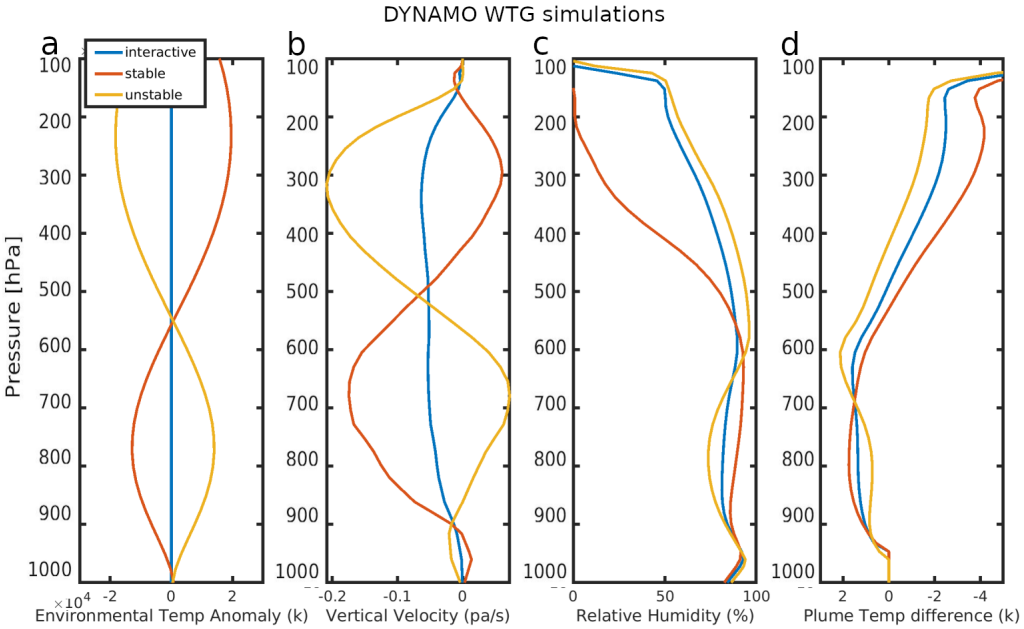

Figure 7. Figure showing test of stability mechanism using variations of the time-mean DYNAMO data and interactive radiation. (a.) The difference in the prescribed SWTG temperature profile between each simulation and the unaltered DYNAMO simulation, which shows the temperature anomalies that are added to the large-scale temperature profiles in order to (de)stabilize them. (b.) The resulting vertical motion profiles. (c.) The relative humidity of all three cases. (d.) The difference in temperature between an entraining plume and the surrounding environment, which measures the buoyancy that a parcel feels and is related to the vertical motion that we simulate. The x-axis has been reversed so that the sign better matches the vertical motion.

5.1 Entraining Plume Buoyancy

Following previous work, we use a simple entraining plume model that follows a parcel leaving the boundary layer. The plume starts its journey with the surface value

of MSE and begins to rise. After it reaches the lifted condensation level (LCL), it begins to lose MSE due to dry air entrainment according to:

$$\frac{\partial h_p}{\partial z} = -\epsilon(h_p - h_e) \tag{9}$$

Here h is the MSE, the p and e denote the parcel and environment respectively. ϵ is the rate that environmental air is entrained. We use a constant rate of 0.25 km^{-1}, because it is simple to analyze and generates buoyancy profiles the most qualitatively similar to the vertical motion profiles for the several rates that we looked at. This assumption could be refined in various ways beyond the scope of our study. We integrate this equation from the LCL to the top of the atmosphere in order to calculate the plume MSE.

We use the difference between the plume MSE and the environmental saturation MSE to calculate the plume buoyancy profile, which is directly related to the large-scale vertical velocity as we will discuss shortly. The difference between the plume temperature and the environment temperature is our measure of buoyancy. We calculate the temperature of the plume, and its difference to the environment, using a Taylor series approximation of the saturation moisture centered at the environmental temperature:

$$h_p^* - h_e^* = c_p\left(T_p - T_e\right) + L_v\left(q_p^* - q_e^*\right) = \left(T_p - T_e\right)\left[c_p + L_v \left.\frac{\partial q^*}{\partial T}\right|_{T_e^*}\right] \tag{10}$$

T is the air temperature, and q is the specific humidity. c_p is the specific heat capacity, L_v is the latent heat of vaporization, and the star superscript represents saturated quantities. We calculate the plume buoyancy by solving this equation, at each level, for the difference in temperature between the plume and the environment.

The plume buoyancy is directly related to the in-cloud vertical motion which is in turn related to the large-scale vertical motion that we are trying to understand. Traditionally, buoyancy is thought to accelerate in-cloud updrafts, but recent research has indicated that buoyancy is directly correlated to the in-cloud vertical motion because plumes rise in a high drag, high friction environment (Romps & Öktem, 2015; Hernandez-Duenas et al., 2019). This means we can qualitatively use the plume buoyancy profile as a proxy for the in-cloud vertical velocity.

The connection between the large-scale vertical motion and the in-cloud mass flux is possible because the large-scale vertical motion is composed of the in-cloud mass flux along with the between cloud subsidence, and cloud fraction according to:

$$\overline{W} = \alpha W_u + (1 - \alpha) W_d \tag{11}$$

Here W is the large-scale vertical motion, W_u is the in-cloud updraft velocity which we represent with the plume buoyancy, and W_d is the between cloud subsidence velocity which is determined by radiative cooling, and α is the cloud fraction.

The in-cloud mass flux changes directly correlate with the large-scale vertical motion as long as the other changes due to the cloud fraction and subsidence rate changes are small. The subsidence velocity is not expected to change dramatically, because that would require a large change in the between cloud radiational cooling rate. Cloud fraction changes could cause in-cloud vertical velocity at each level to not correlate with large-scale vertical motion, but for the purposes of this work we neglect that effect. Further refinements to our conceptual model that are beyond the scope of this work could be made by relating cloud fraction at each level to humidity at that level.

The simulations that validated the WTG model's representation of the stability mechanism provide an excellent test case for whether the entraining plume model can

describe why the more stable case has a more bottom-heavy vertical motion profile, and we find that it does. The simulations of interest are simulations 1-3, and the only difference between the three simulations were the temperature anomalies that we added, shown in Figure (6a), which created large differences in the WTG velocity. We calculate the plume buoyancy for each of these simulations and show these in figure (7 d) along with the WTG vertical motion, relative humidity, and the temperature anomaly.

The differences between the buoyancy profiles is qualitatively similar to the differences between the vertical motion profiles. The test case with the stabilizing anomaly, the orange line in Figure (7), shows a more bottom-heavy vertical motion profile in the SWTG simulations (figure 7 b.) and the entraining plume buoyancy profile is more bottom heavy than the control case (figure 7 a.). The destabilizing anomaly leads to a more top-heavy vertical motion profile in the SWTG simulations and the entraining plume has a more top-heavy buoyancy profile. The simplicity of the model and its assumptions means we do not expect a close quantitative match, and the closeness of the qualitative match shows the model works well for our purposes and supports our idea that the plume model provides a useful explanation of what we observed in the cloud resolving model simulations.

5.2 Sensitivity Results

The entraining plume has shown good qualitative results and captures the stability mechanism, so we next turn the model to the sensitivity simulation results to better understand the reason for our top-heaviness difference. We calculate the temperature profiles used in the buoyancy calculations by averaging the domain mean temperature from every simulation with the chosen common parameter. For instance, if we are interested in the effect of the bottom-heavy temperature we average all of the simulations that used the bottom-heavy temperature profile, which gives us the temperature profile differences attributable to using the bottom-heavy temperature profile in WTG simulations. We calculate the moisture profile using the RH from either the basic top or bottom-heavy simulation along with the temperature profile that we just calculated. We additionally wish to test the effect of only the temperature differences, so we also calculate the buoyancies using the mean RH from the two basic simulations.

We are further interested in the relative effect between the top and bottom-heavy box, so we subtract the two cases giving us the effect due to switching a variable. We select the order of subtraction in order to highlight a particular change. For the stability we choose the order so that it represents a change from the top-heavy to bottom-heavy case and for the rest we choose the order so that it is a change from bottom to top heavy.

Figure (6 b) shows the plume buoyancy difference with the effect of moisture included. We have flipped the sign from normal convention so that it aligns with pressure velocity changes. The two largest buoyancy effects, in line with the vertical motion, are due to changes in the SST and stability. The qualitative difference between the vertical motion profiles and buoyancy profiles are strikingly similar, with an increased bottom-heaviness due to stability changes and an increased top-heaviness due to SST changes. The upper troposphere effects are much more pronounced and exaggerated due to the SST changes. The other two effects that we test, moisture advection and radiation, seem to drive a negative buoyancy anomaly that is very small.

When we remove the effects of differing RH profiles between the two boxes, we see distinct buoyancy changes (figure 6 c). The stability creates the largest increase in plume buoyancy, however the SST shows negative buoyancy changes. The difference between the two buoyancy effects still resembles the vertical motion profile difference that we see, more buoyancy near the surface in the stability case and less buoyancy in the upper troposphere, but the profiles are much less similar when moisture is not included.

The effect of the SST on the buoyancy can only be seen when the RH differences are included because the WTG parameterization precludes the existence of the temperature profile changes that would be needed in order to change the buoyancy. The stability sensitivity also became more bottom heavy. This is consistent with the stability validation results, which showed that the stability changes led to moisture changes which act to reinforce the buoyancy and therefore top-heaviness differences. When a temperature change instigates a buoyancy change the effect is also moderated by the moisture and therefore an accurate moisture parameterization is essential to capturing the buoyancy and vertical motion profile that result.

The simple entraining plume model that we have presented here has captured how aspects of both the stability and dynamic mechanisms operate. Changing the stability of the atmosphere affects the top-heaviness by changing the buoyancy that plumes feel as they rise. Higher SSTs drive greater vertical motion by increasing the starting energy and buoyancy that a plume feels.

Figure (8) shows a visualization of the changes the SST, stability and moisture have on the buoyancy and thus the vertical motion. The toy model is created by initializing the environment with a starting temperature and constant lapse rate. The moisture is then determined by a constant RH value for the boundary layer and the free troposphere. The temperature and moisture changes are created by increasing the MSE, in the case of the moisture, and the MSE and saturated MSE, in the case of the temperature, by 2K equivalent, in a small layer lower in the atmosphere. The SST change is accomplished by increasing the MSE that the plume starts with by 2K.

The moisture increase (see figure 8 a) leads to an increase in the buoyancy above where the moisture is changed. The temperature increase (see figure 8 b), has two effects, the first is identical to the moisture increase, because we have increased the temperature while maintaining the RH constant. The second effect is a local decrease in the buoyancy because the saturated MSE of the environment has increased, which means the latent energy of the parcel goes into achieving saturation instead of being excess buoyancy. Increasing the SST (see figure 8 c) leads to an increase in the buoyancy throughout the column.

This toy model demonstrates the basic changes on buoyancy and vertical motion due to idealized changes in the thermodynamic state. The real atmosphere operates in a similar, albeit more complicated, fashion and the toy model provides a simplified explanation of a complex system. The toy model shows higher SSTs and more environmental moisture increases buoyancy and a positive temperature anomaly leads to a negative buoyancy anomaly. We expect these same relationships to be seen in the real atmosphere, although the toy model offers no predictions to specifics of the relationship. We now move on to reconciling our two mechanisms into a more cohesive understanding of what controls climatological top-heaviness.

6 Reconciling the two mechanisms

We have shown that we are able to simulate bottom-heavy vertical motion without the imposition of SST gradients or a surface convergence. The sensitivity simulations and entraining plume model revealed that the most important thermodynamic factors were the temperature profile and underlying SST. Combining these facts with the predictive power demonstrated by the dynamic mechanism leads to the natural conclusion that the dynamic mechanism acts through the stability mechanism. This agrees with prior research by Raymond (2017), who found that the Ekman convergence did not explain all the variability on daily time scales. In order to join the two mechanisms, we look at how the dynamic mechanism can interact with the stability mechanism via the temperature profile.

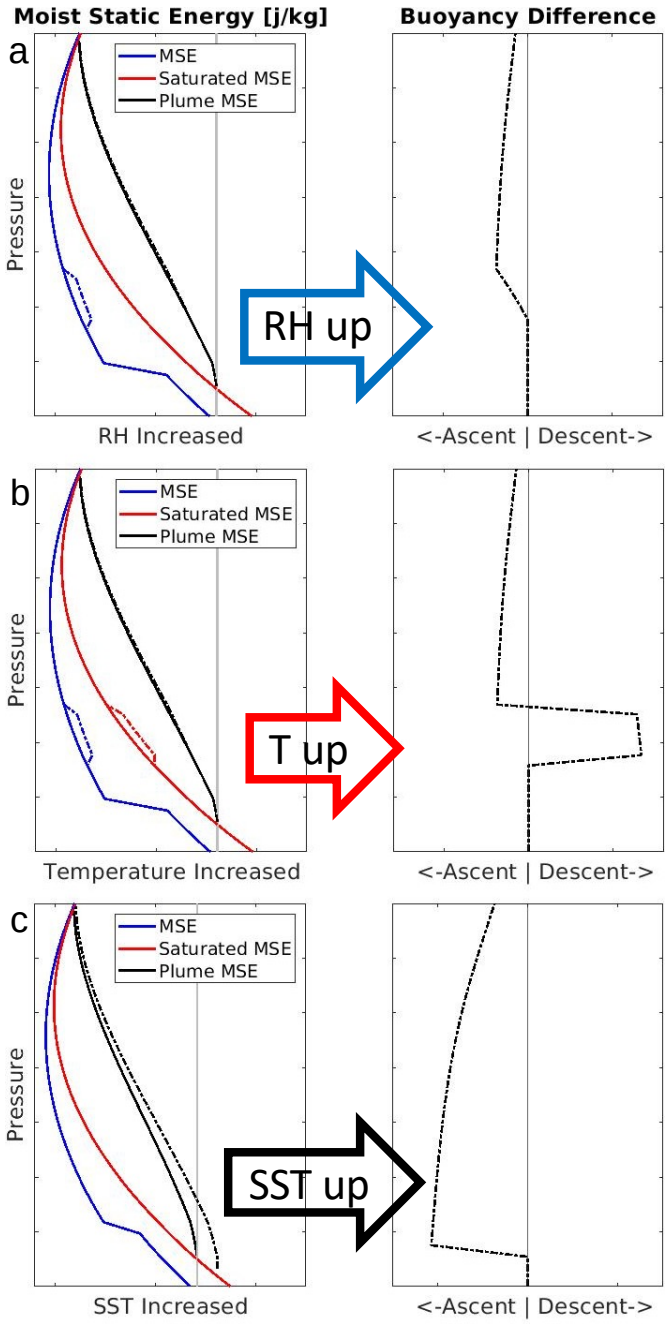

Figure 8. Figure showing the basic effect that changing the environmental temperature, moisture, or SST have on the buoyancy of an entraining plume. The solid lines show an unmodified example case and the dashed line shows a modification to either the temperature or moisture. The panels on the right show the difference in plume buoyancy between the two cases shown on the left. (a.) The Moisture change is created by increasing the MSE that the plume entrains by the equivalent of 2K over a small layer lower in the atmosphere. This change results in a small increase in the buoyancy above the change. (b.) The temperature change shown is also 2K and is over the same short layer lower in the atmosphere. In addition to the moisture change from increasing the temperature and holding the RH constant, there is the local decrease in buoyancy due to the increase in the saturation moisture with the temperature increase. (c.) Increase in the SST is demonstrated by increasing the initial temperature of the plume by 2K.

The primary way that the two mechanisms interact is through the dependence of the temperature profile, and thus stability, on the SST. Because of the large Rossby radius of deformation in the tropics, the temperature profile above the boundary layer is constantly relaxing towards the tropical mean due to the effects of gravity wave propagation. For there to be differences in the temperature profile on climatological scales there must be a consistent source of heating difference that is strong enough to counteract the effects of gravity wave propagation. SST differences are the largest source of heating difference, which influence the levels closest to the surface the most. The stability of the temperature profile can be simplified by describing it as the slope of the lapse rate between the surface and mid-levels. The mid-level temperature gradients are negligible and the surface temperature variations are predominantly determined by the local SST, so the variance of the temperature profile is controlled by the underlying SST. This can be seen in the temperature differences in figure (4), which shows a more stable temperature profile over the cooler SST of the bottom-heavy box.

Next we check the relationship between the stability and SST in our two boxes more broadly. To do this, we utilize the instability index (II) as our measure of stability of the temperature profile and stability. The II has been used previously during research of the stability mechanism and is defined as the difference of the mean saturation moist static entropy between the lower troposphere, defined from 1 to 3 km, and the middle troposphere, defined from 5 to 7 km (Raymond et al., 2015; Sessions et al., 2019). We plot the mean II and SST for every month that comprises our climatology in figure 9, where smaller values for the II correspond to more stable profiles. Each marker is shaped according to which box it is from and is colored according to the top-heaviness angle color map in figure (1) to show their combined relationship with the monthly top-heaviness angle.

There is a general correlation of higher SSTs, less stable temperature profiles, and top-heavier vertical motion. These trends are strongly dominated by both the behavior within top-heavy boxes along with the relative differences between the two boxes. The correlations between SST and stability as well as between SST and top-heaviness are missing from the bottom-heavy box. However, for each group of SSTs, an increase in the II corresponds to an increase in the top heaviness. The general trend shows that the stability predicts the top-heaviness and in the top-heavy box the stability, and thus the top-heaviness, is predicted by the SST. Something else appears to be controlling the stability and the top-heaviness in the bottom-heavy box.

We hypothesize that the stability in the bottom-heavy box is influenced by the gradients of SST that are central to the dynamic mechanism's successful prediction of bottom-heavy vertical motion. This process is shown in figure 10. The mechanism initially acts as before: SST gradients imprint on the boundary layer creating bent isobars which act in conjunction with surface friction to drive a surface convergence and vertical motion. This vertical motion, because it is driven by SST gradients and not diabatic heating, leads to a relatively cooler temperature over the same magnitude SST with no gradient. Singh et al. (2019b) showed that increasing vertical motion led to lower temperatures in a CRM and a bulk plume model. The dynamic mechanism appears to exert its control over the top-heaviness through the stability mechanism and the thermodynamics.

Using the entraining plume framework and reconciling the two mechanisms gives us a description of the controls over the vertical motion profile shape. Starting with the temperature profile without additional context, the increased stability in the Central-Eastern Pacific, characterized by a lower lapse rate, leads to bottom-heavy vertical motion because it increases the plume buoyancy near the surface which increases the vertical motion. The lower local magnitude of the SST in the central Eastern Pacific leads to less plume buoyancy and vertical motion relative to the Western Pacific. The relative difference in the SST is important to the stability differences between the two regions because the mid-level temperature across the tropics varies less compared to the

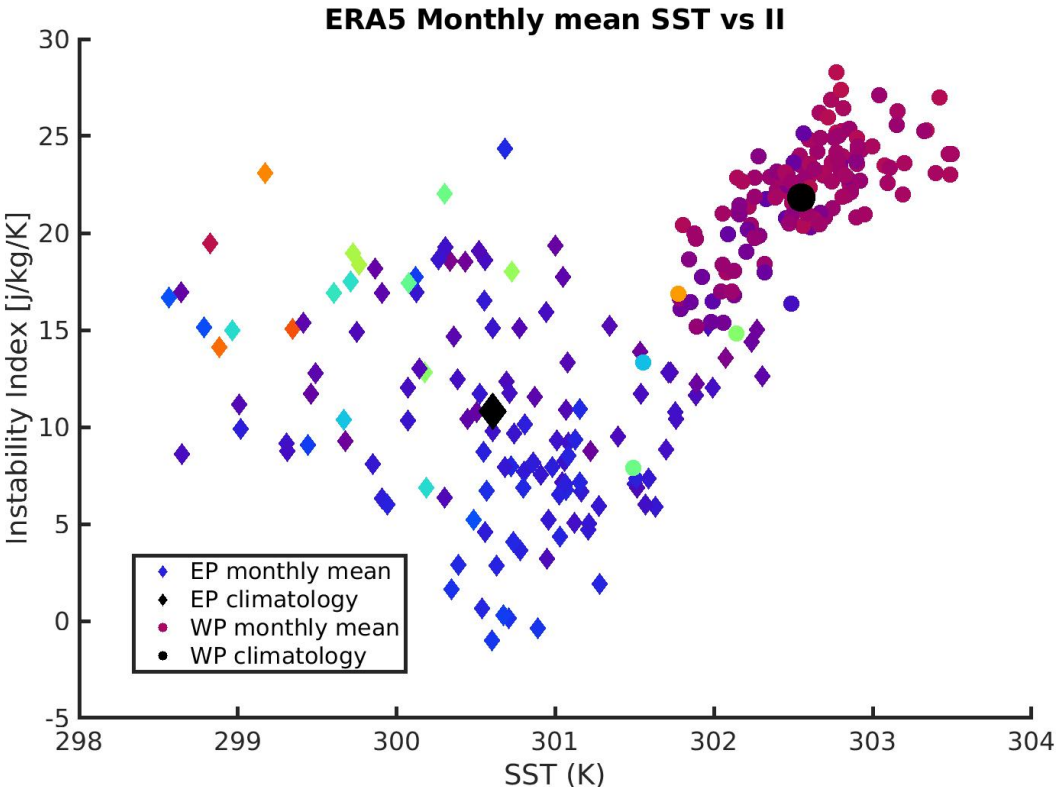

Figure 9. Comparison of the relationship between the stability and SST in each of our two regions and how these relate to vertical motion shape changes. Scatter plot of the II (a measure of temperature stratification) and SST from ERA5 climatology data. Each point is a monthly mean from the climatology that we use to simulate the East and West Pacific. The East and West Pacific are differentiated with different markers. Each point is colored according to the top-heaviness angle from that month. The legend for top-heaviness angle can be found in figure (1).

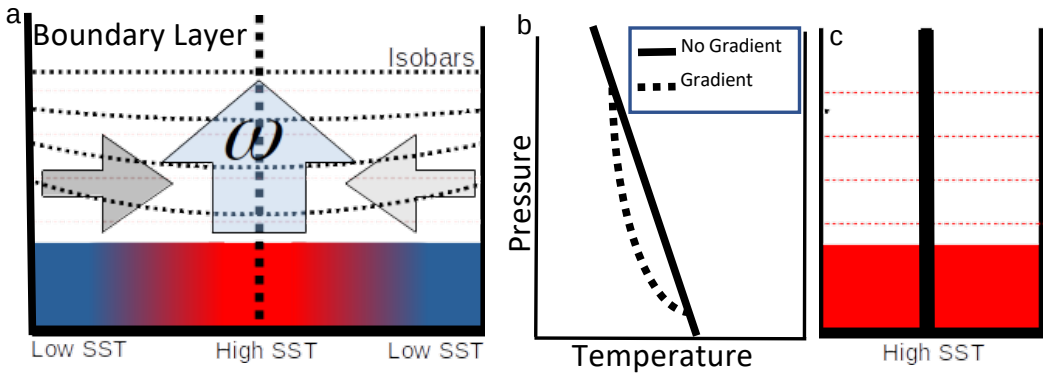

Figure 10. Schematic of how we hypothesize the dynamic mechanism influences the stability mechanism by changing the stability. (a.) The SST gradients in association with friction drive the convergent winds. The mass-continuity associated vertical motion leads to a climatological temperature profile that is cooler than it would be without convergent winds. The vertical motion that is imposed by the SST gradients and friction lead to a temperature profile that is more stable. (b.) The temperature profiles for the case with SST gradients and without are shown. (c.) The schematic showing the case of no SST gradients.

surface temperature, which leads to the atmosphere over the warmer SSTs in the Western Pacific to be less stable. Finally, we posit that the SST gradients in the Central-Eastern Pacific, and their associated near surface vertical motion, act to cool and stabilize the temperature profile beyond what the SST alone would lead to, which also contributes to vertical motion that is more bottom heavy.

7 Horizontal Advection and MQE

A key result in the establishment of the stability mechanism, and the related process of moisture quasi-equilibrium (MQE), is the relationship between column moisture, dry static stability, and top-heaviness (Gjorgjievska & Raymond, 2014; Sentić et al., 2015; Sessions et al., 2015, 2019). These research efforts demonstrate that the stability, column moisture, and vertical motion are related to each other due to MQE. The simulations we ran for validation, for our comparison of the two boxes, and in the reanalysis data of the two boxes do not show a relationship between the top-heaviness and column moisture. We hypothesize that the lack of correlation is due to how the horizontal moisture advection occurs in each context and it highlights the importance of horizontal moisture advection to the behavior of MQE.

The descriptions of the stability-moisture relationship have used vertical motion to explain the mediation, and specifically the horizontal moisture advection due to the divergence field associated with the vertical motion. Wang et al. (2016) showed that, during the DYNAMO campaign, the observed horizontal moisture advection could not be adequately captured by the local divergence field. The lateral entrainment scheme models the moisture advection due to the local divergence field and so Wang et al. (2016) chose to instead parameterize moisture advection by imposing the profile from observation. We similarly choose to impose the profile of moisture advection instead of using a lateral entrainment scheme which differentiates our simulations from those previous which showed the stability moisture relationship.

We hypothesize that the stability moisture relationship is not present in our simulations because we imposed the horizontal moisture advection, which eliminates an im-

portant additional feedback to moisture from the horizontal moisture advection. The stability mechanism, and MQE, describe the relationship between stability and moisture as being moderated by the vertical motion and the net MSE import or export (Raymond et al., 2015). The relationship between column moisture and vertical motion shape is dependent upon strong feedbacks between them, which can be disrupted, for example, by a strong non-local source of horizontal moisture advection dominating variability. Hence, we expect to see the strength of signal between stability, moisture, and vertical motion profile shape increase when horizontal advection is dominated by local sources.

8 Conclusion

We have, using a spectral WTG approximation, simulated the top and bottom-heavy vertical motion profile shapes from two regions in the Western and Central-Eastern Pacific. Through these simulations we have uncovered that:

- The vertical motion shape differences in our regions of interest are a consequence primarily of the temperature profile and SST differences.
- A simple entraining plume model captures the thermodynamic and the control of the stability mechanism over the top-heaviness of vertical motion.
- The dynamic mechanism likely acts through the stability mechanism, allowing us to reconcile our two mechanisms.
- The correlation between dry static stability and column water vapor in the stability mechanism requires the horizontal moisture advection be primarily determined by local divergence.

We have shown that the most important differences to the top-heaviness between our two boxes are the large-scale temperature profile and the SST. The bottom-heavy vertical motion in the Eastern Pacific is due to a combination of its relatively low SST and high dry static stability, while the top-heavy vertical motion in the Western Pacific can be attributed to its higher SST and its less stable temperature profile.

The two explanations for the controls of top-heaviness, the dynamic mechanism and stability mechanisms, can be reconciled by the dynamic mechanism controlling the top-heaviness through its influence over the stability mechanism. The SST distribution, which lies at the heart of the dynamic mechanism explanation, imparts its control over vertical motion through its influence on the local dry static stability. The magnitude of the local SST sets the local temperature near the surface and that temperature control decreases with height, due to the lack of rotation. The column with the greater SST cools more quickly with height to reach the same temperature in the mid-levels, which leads to a greater lapse rate and more unstable atmosphere. However, we showed that this does not explain the month-to-month stability differences that we observe in the central Eastern Pacific. We hypothesize that the surface convergence due to SST gradient acts to cool and stabilize the atmosphere, which also leads to an increase in the bottom-heaviness of vertical motion. We argue that the month-to-month stability variations in the Central-Eastern Pacific are caused by cooling attributed to SST gradient driven surface convergence.

We have also shown that the qualitative vertical motion changes can be captured by the simple model of an entraining plume. The stability validation simulations showed that the differences between the simulated WTG vertical motion profiles looked qualitatively similar to the plume buoyancy differences that were calculated from the simulated moisture and temperature profiles. Applying a temperature anomaly led to both vertical motion and moisture profile changes. Additionally, the buoyancy differences induced by changing the SST were primarily due to moisture profile differences and not

temperature profile differences. This highlights the need to understand the profile of moisture and how it interacts with the top-heaviness of vertical motion.

We have also shown the strength of the relationship between stability and column water vapor depends upon the horizontal advection being forced by the local vertical velocity and moisture. When considered narrowly this indicates that the large difference in top-heaviness between our two boxes occurring without large column moisture and precipitation differences is attributed to the differences in the moisture of the surrounding environment. On a broader scale, this means that the stability-moisture relationship from MQE and the stability mechanism can be reduced and disappear if the non-local processes drive counter horizontal moisture advective variations. Larger storms in higher vorticity environments, such as the storms undergoing cyclogenesis from Gjorgjievska and Raymond (2014), are expected to strongly exhibit MQE as previously described. Future research is needed to understand where these relations can be safely applied.

The research presented here demonstrates the need to understand the thermodynamic environment in order to predict the vertical motion profile. The temperature profile plays a key role in moderating the relationship between vertical motion and moisture, and the SST distribution enforces vertical motion changes through the temperature profile. We can apply this newly gained understanding to tropical forecasting and modeling efforts in order to diagnose and fix our representations of the important processes.

Open Research Section

ERA5 reanalysis data was obtained from the Copernicus Data Store (CDS) for both the data on pressure levels (Hersbach et al., 2019a) and single levels (Hersbach et al., 2019b) on June 30, 2020. The simulation outputs and and scripts used to produce the figures are published and available at `https://github.com/mbernard3605/Bernardez_JAMES_data/` (Bernardez, 2022). See the README for instructions on how to use the scripts and detailed explanations of each of the files. We used WRF (v3.5.1) (Skamarock et al., 2008) and the WTG parameterization is described in detail in (Wang et al., 2016) and the authors of that paper should be approached for their parameterization.

Acknowledgments
We thank Quinn Bowman, Stipo Sentic, and two anonymous reviewers for their invaluable constructive criticism. We also thank Shuguang Wang for the use of their model. This work was supported by NSF Award #1759793 and the advanced opportunity fellowship.

References

Abbott, T. H., & Cronin, T. W. (2021). Aerosol invigoration of atmospheric convection through increases in humidity. *Science*, *371*(6524), 83–85. doi: 10.1126/science.abc5181

Adames, Á. F., Powell, S. W., Ahmed, F., Mayta, V. C., & Neelin, J. D. (2021, feb). Tropical Precipitation Evolution in a Buoyancy-Budget Framework. *Journal of the Atmospheric Sciences*, *78*(2), 509–528. Retrieved from `https://journals.ametsoc.org/view/journals/atsc/78/2/jas-d-20-0074.1.xml` doi: 10.1175/JAS-D-20-0074.1

Ahmed, F., & Neelin, J. D. (2018). Reverse engineering the tropical precipitation-buoyancy relationship. *Journal of the Atmospheric Sciences*, *75*(5), 1587–1608. doi: 10.1175/JAS-D-17-0333.1

Anber, U., Gentine, P., Wang, S., & Sobel, A. H. (2015). Fog and rain in the Amazon. *Proceedings of the National Academy of Sciences of the United States of*

America, *112*(37), 11473–11477. doi: 10.1073/pnas.1505077112

Arakawa, A., & Schubert, W. H. (1974, apr). Interaction of a Cumulus Cloud Ensemble with the Large-Scale Environment, Part I. *Journal of the Atmospheric Sciences*, *31*(3), 674–701. Retrieved from http://journals.ametsoc.org/doi/10.1175/1520-0469(1974)031%3C0674:IOACCE%3E2.0.CO;2 doi: 10.1175/1520-0469(1974)031⟨0674:IOACCE⟩2.0.CO;2

Back, L. E., & Bretherton, C. S. (2006). Geographic variability in the export of moist static energy and vertical motion profiles in the tropical Pacific. *Geophysical Research Letters*, *33*(17), 1–5. doi: 10.1029/2006GL026672

Back, L. E., & Bretherton, C. S. (2009a). On the relationship between SST gradients, boundary layer winds, and convergence over the tropical oceans. *Journal of Climate*, *22*(15), 4182–4196. doi: 10.1175/2009JCLI2392.1

Back, L. E., & Bretherton, C. S. (2009b). A simple model of climatological rainfall and vertical motion patterns over the tropical oceans. *Journal of Climate*, *22*(23), 6477–6497. doi: 10.1175/2009JCLI2393.1

Back, L. E., Hansen, Z., & Handlos, Z. (2017). Estimating Vertical Motion Profile Top-Heaviness: Reanalysis Compared to Satellite-Based Observations and Stratiform Rain Fraction. *Journal of the Atmospheric Sciences*, *74*(3), 855–864. doi: 10.1175/jas-d-16-0062.1

Bernardez, M. (2022). *Data files and matlab scripts used for this paper* [software]. doi: 10.5281/zenodo.7186525

Bretherton, C. S., Peters, M. E., & Back, L. E. (2004). Relationships between water vapor path and precipitation over the tropical oceans. *Journal of Climate*, *17*(7), 1517–1528. doi: 10.1175/1520-0442(2004)017⟨1517:RBWVPA⟩2.0.CO;2

Chou, M.-D., & Suarez, M. J. (1999). *A solar radiation parameterization for atmospheric studies* (Tech. Rep.).

Ciesielski, P. E., Yu, H., Johnson, R. H., Yoneyama, K., Katsumata, M., Long, C. N., ... others (2014). Quality-controlled upper-air sounding dataset for dynamo/cindy/amie: Development and corrections. *Journal of Atmospheric and Oceanic Technology*, *31*(4), 741–764.

Daleu, C. L., Plant, R. S., Woolnough, S. J., Sessions, S., Herman, M. J., Sobel, A., ... Van Ulft, L. (2015). Intercomparison of methods of coupling between convection and large-scale circulation: 1. Comparison over uniform surface conditions. *Journal of Advances in Modeling Earth Systems*, *7*(4), 1576–1601. doi: 10.1002/2015MS000468

Duffy, M. L., O'Gorman, P. A., & Back, L. E. (2020). Importance of Laplacian of Low-Level Warming for the Response of Precipitation to Climate Change over Tropical Oceans. *Journal of Climate*, *33*(10), 4403–4417. Retrieved from https://journals.ametsoc.org/jcli/article/33/10/4403/345259/Importance-of-Laplacian-of-LowLevel-Warming-for doi: 10.1175/JCLI-D-19-0365.1

Edman, J. P., & Romps, D. M. (2015, mar). Self-consistency tests of large-scale dynamics parameterizations for single-column modeling. *Journal of Advances in Modeling Earth Systems*, *7*(1), 320–334. Retrieved from https://onlinelibrary.wiley.com/doi/10.1002/2014MS000378 doi: 10.1002/2014MS000378

Gjorgjievska, S., & Raymond, D. J. (2014). Interaction between dynamics and thermodynamics during tropical cyclogenesis. *Atmospheric Chemistry and Physics*, *14*(6), 3065–3082. doi: 10.5194/acp-14-3065-2014

Hagos, S., Zhang, C., Tao, W. K., Lang, S., Takayabu, Y. N., Shige, S., ... L'ecuyer, T. (2010). Estimates of tropical diabatic heating profiles: Commonalities and uncertainties. *Journal of Climate*, *23*(3), 542–558. doi: 10.1175/2009JCLI3025.1

Handlos, Z. J., & Back, L. E. (2014). Estimating vertical motion profile shape within tropical weather states over the oceans. *Journal of Climate*, *27*(20),

7667–7686. doi: 10.1175/JCLI-D-13-00602.1

Herman, M. J., & Raymond, D. J. (2014). WTG cloud modeling with spectral decomposition of heating. *Journal of Advances in Modeling Earth Systems*, *6*(4), 1121–1140. doi: 10.1002/2014MS000359

Hernandez-Duenas, G., Smith, L. M., & Stechmann, S. N. (2019). Weak- and strong-friction limits of parcel models: Comparisons and stochastic convective initiation time. *Quarterly Journal of the Royal Meteorological Society*, *145*(722), 2272–2291. doi: 10.1002/qj.3557

Hersbach, H., Bell, P., B. Berrisford, Biavati, G., Horányi, A., Muñoz Sabater, J., Nicolas, J., ... Thépaut, J.-N. (2019a). *Era5 monthly averaged data on pressure levels from 1979 to present. copernicus climate change service (c3s) climate data store (cds)* [dataset]. (Accessed: 2019-06) doi: 10.24381/cds.6860a573

Hersbach, H., Bell, P., B. Berrisford, Biavati, G., Horányi, A., Muñoz Sabater, J., Nicolas, J., ... Thépaut, J.-N. (2019b). *Era5 monthly averaged data on single levels from 1959 to present. copernicus climate change service (c3s) climate data store (cds)* [dataset]. (Accessed: 2019-06) doi: 10.24381/cds.f17050d7

Iacono, M. J., Delamere, J. S., Mlawer, E. J., Shephard, M. W., Clough, S. A., & Collins, W. D. (2008). Radiative forcing by long-lived greenhouse gases: Calculations with the aer radiative transfer models. *Journal of Geophysical Research: Atmospheres*, *113*(D13).

Inoue, K., Adames, Á. F., & Yasunaga, K. (2020). Vertical velocity profiles in convectively coupled equatorial waves and mjo: New diagnoses of vertical velocity profiles in the wavenumber–frequency domain. *Journal of the Atmospheric Sciences*, *77*(6), 2139–2162.

Inoue, K., & Back, L. (2015). Column-integrated moist static energy budget analysis on various time scales during TOGA COARE. *Journal of the Atmospheric Sciences*, *72*(5), 1856–1871. doi: 10.1175/JAS-D-14-0249.1

Johnson, R. H., & Ciesielski, P. E. (2013). Structure and properties of madden–julian oscillations deduced from dynamo sounding arrays. *Journal of the Atmospheric Sciences*, *70*(10), 3157–3179.

Kang, S. M., Frierson, D. M., & Held, I. M. (2009). The tropical response to extratropical thermal forcing in an idealized GCM: The importance of radiative feedbacks and convective parameterization. *Journal of the Atmospheric Sciences*, *66*(9), 2812–2827. doi: 10.1175/2009JAS2924.1

Klemp, J. B., Dudhia, J., & Hassiotis, A. D. (2008). An upper gravity-wave absorbing layer for nwp applications. *Monthly Weather Review*, *136*(10), 3987 - 4004. Retrieved from `https://journals.ametsoc.org/view/journals/mwre/136/10/2008mwr2596.1.xml` doi: https://doi.org/10.1175/2008MWR2596.1

Lindzen, R. S., & Nigam, S. (1987). On the Role of Sea Surface Temperature Gradients in Forcing Low-Level Winds and Convergence in the Tropics. *Journal of the Atmospheric Sciences*, *44*(17), 2418–2436. doi: 10.1175/1520-0469(1987)044⟨2418:otross⟩2.0.co;2

Madden, R. A., & Julian, P. R. (1971). Detection of a 40–50 day oscillation in the zonal wind in the tropical pacific. *Journal of Atmospheric Sciences*, *28*(5), 702–708.

Maloney, E. D., Gettelman, A., Ming, Y., Davidneelin, J., Barrie, D., Mariotti, A., ... Zhao, M. (2019). Process-oriented evaluation of climate and weather forecasting models. *Bulletin of the American Meteorological Society*, *100*(9), 1665–1686. doi: 10.1175/BAMS-D-18-0042.1

Matsui, T., Tao, W., & Shi, R. (2007). Goddard radiation and aerosol direct effect in goddard wrf. In *Nasa/umd wrf workshop*.

Morrison, H., Thompson, G., & Tatarskii, V. (2009). Impact of cloud microphysics on the development of trailing stratiform precipitation in a simulated squall line: Comparison of one-and two-moment schemes. *Monthly weather review*,

137(3), 991–1007.

Raymond, D. J. (2017). Convection in the east Pacific Intertropical Convergence Zone. *Geophysical Research Letters*, *44*(1), 562–568. doi: 10.1002/2016GL071554

Raymond, D. J., & Flores, M. M. (2016). Predicting convective rainfall over tropical oceans from environmental conditions. *Journal of Advances in Modeling Earth Systems*, *8*, 703–718. doi: 10.1002/2013MS000595

Raymond, D. J., Fuchs, Ž., Gjorgjievska, S., & Sessions, S. L. (2015). Balanced dynamics and convection in the tropical troposphere. *Journal of Advances in Modeling Earth Systems*, *7*, 1093–1116. doi: 10.1002/2013MS000467

Raymond, D. J., & Fuchs-Stone. (2021). Weak Temperature Gradient Modeling of Convection in OTREC. *Journal of Advances in Modeling Earth Systems*, *13*(10). doi: 10.1029/2021MS002557

Raymond, D. J., S, G., S, S., Z, F., Gjorgjievska, S., & Sessions, S. (2014). Tropical Cyclogenesis and Mid-Level Vorticity. *Australian Meteorological and Oceanographic Journal*, *64*, 1–30.

Raymond, D. J., & Sessions, S. L. (2007). Evolution of convection during tropical cyclogenesis. *Geophysical Research Letters*, *34*(6), 1–11. doi: 10.1029/2006GL028607

Raymond, D. J., & Zeng, X. (2005). Modelling tropical atmospheric convection in the context of the weak temperature gradient approximation. *Quarterly Journal Of The Royal Meteorological Society*, *131*(608), 1301–1320. Retrieved from `http://doi.wiley.com/10.1256/qj.03.97%5Cnpapers2://publication/doi/10.1256/qj.03.97` doi: 10.1256/qj.03.97

Riehl, H., & Malkus, J. S. (1958). On the heat balance of the equatorial trough zone. *Geophysica*, *6*, 503–538.

Romps, D. M. (2021). Ascending columns, WTG, and convective aggregation. *Journal of the Atmospheric Sciences*, *78*(2), 497–508. doi: 10.1175/JAS-D-20-0041.1

Romps, D. M., & Öktem, R. (2015). Stereo photogrammetry reveals substantial drag on cloud thermals. *Geophysical Research Letters*, *42*(12), 5051–5057. doi: 10.1002/2015GL064009

Schumacher, C., Houze, R. A., & Kraucunas, I. (2004). The tropical dynamical response to latent heating estimates derived from the TRMM precipitation radar. *Journal of the Atmospheric Sciences*, *61*(12), 1341–1358. doi: 10.1175/1520-0469(2004)061⟨1341:TTDRTL⟩2.0.CO;2

Sentić, S., Sessions, S. L., & Fuchs, Ž. (2015, dec). Diagnosing DYNAMO convection with weak temperature gradient simulations. *Journal of Advances in Modeling Earth Systems*, *7*(4), 1849–1871. Retrieved from `http://doi.wiley.com/10.1002/2015MS000531` doi: 10.1002/2015MS000531

Sessions, S. L., Herman, M. J., & Sentić, S. (2015). Convective response to changes in the thermodynamic environment in idealized weak temperature gradient simulations. *Journal of Advances in Modeling Earth Systems*, *7*, 712–738. doi: 10.1002/2013MS000282.Received

Sessions, S. L., Sentic, S., & Herman, M. J. (2016). The role of radiation in organizing convection in weak temperature gradient simulations. *Journal of Advances in Modeling Earth Systems*, *8*(1), 244–271. doi: 10.1002/2015MS000587

Sessions, S. L., Sentić, S., & Raymond, D. J. (2019). Balanced Dynamics and Moisture Quasi-Equilibrium in DYNAMO Convection. *Journal of the Atmospheric Sciences*, *76*(9), 2781–2799. doi: 10.1175/jas-d-18-0173.1

Sherwood, S. C., Bony, S., & Dufresne, J. L. (2014). Spread in model climate sensitivity traced to atmospheric convective mixing. *Nature*, *505*(7481), 37–42. doi: 10.1038/nature12829

Shi, J. J., Tao, W.-K., Matsui, T., Cifelli, R., Hou, A., Lang, S., ... others (2010). Wrf simulations of the 20–22 january 2007 snow events over eastern canada:

Comparison with in situ and satellite observations. *Journal of Applied Meteorology and Climatology*, *49*(11), 2246–2266.

Singh, M. S., & Neogi, S. (2022). On the Interaction between Moist Convection and Large-Scale Ascent in the Tropics. *Journal of Climate*, *35*(14), 4417–4435. doi: 10.1175/JCLI-D-21-0717.1

Singh, M. S., & O'Gorman, P. A. (2013). Influence of entrainment on the thermal stratification in simulations of radiative-convective equilibrium. *Geophysical Research Letters*, *40*(16), 4398–4403. doi: 10.1002/grl.50796

Singh, M. S., Warren, R. A., & Jakob, C. (2019a). A Steady-State Model for the Relationship Between Humidity, Instability, and Precipitation in the Tropics. *Journal of Advances in Modeling Earth Systems*, *11*(12), 3973–3994. doi: 10.1029/2019MS001686

Singh, M. S., Warren, R. A., & Jakob, C. (2019b). A Steady-State Model for the Relationship Between Humidity, Instability, and Precipitation in the Tropics. *Journal of Advances in Modeling Earth Systems*, *11*(12), 3973–3994. doi: 10.1029/2019MS001686

Skamarock, W. C., Klemp, J. B., Dudhia, J., Gill, D. O., Barker, D. M., Duda, M. G., ... Powers, J. G. (2008). *A Description of the Advanced Research WRF Version 3* (Tech. Rep.). University Corporation for Atmospheric Research. (Note NCAR/TN-468+ STR)

Sobel, A. H., Bellon, G., & Bacmeister, J. (2007). Multiple equilibria in a single-column model of the tropical atmosphere. *Geophysical Research Letters*, *34*(22), 1–5. doi: 10.1029/2007GL031320

Sobel, A. H., & Bretherton, C. S. (2000). Modeling tropical precipitation in a single column. *Journal of Climate*, *13*(24), 4378–4392. doi: 10.1175/1520-0442(2000)013⟨4378:MTPIAS⟩2.0.CO;2

Sobel, A. H., Nilsson, J., & Polvani, L. M. (2001). The Weak Temperature Gradient Approximation and Balanced Tropical Moisture Waves*. *Journal of the Atmospheric Sciences*, *58*(23), 3650–3665. doi: 10.1175/1520-0469(2001)058⟨3650:TWTGAA⟩2.0.CO;2

Wang, S., & Sobel, A. H. (2012). Impact of imposed drying on deep convection in a cloud-resolving model. *Journal of Geophysical Research Atmospheres*, *117*(2), 1–14. doi: 10.1029/2011JD016847

Wang, S., Sobel, A. H., & Kuang, Z. (2013). Cloud-resolving simulation of TOGA-COARE using parameterized large-scale dynamics. *Journal of Geophysical Research Atmospheres*, *118*(12), 6290–6301. doi: 10.1002/jgrd.50510

Wang, S., Sobel, A. H., & Nie, J. (2016). Modeling the MJO in a cloud-resolving model with parameterized large-scale dynamics: Vertical structure, radiation, and horizontal advection of dry air. *Journal of Advances in Modeling Earth Systems*, *8*(1), 121–139. doi: 10.1002/2015MS000529

Yanai, M., Esbensen, S., & Chu, J.-H. (1973). Determination of Bulk Properties of Tropical Cloud Clusters from Large-Scale Heat and Moisture Budgets. *Journal of the Atmospheric Sciences*, *30*(4), 611–627. doi: 10.1175/1520-0469(1973)030⟨0611:DOBPOT⟩2.0.CO;2